Supporting Information:

Is DFT enough? Towards Accurate High-Throughput Computational Screening of Azobenzenes for Molecular Solar Thermal Applications

Flavia Aleotti,* Lorenzo Soprani, Lucas F. Rodríguez-Almeida, Francesco Calcagno, Fabio Loprete, Ivan Rivalta, Silvia Orlandi, Elisabetta Canè, Marco Garavelli,* Irene Conti,* and Luca Muccioli*

Dipartimento di Chimica Industriale "Toso Montanari", University of Bologna, Via Gobetti 85, 40129 Bologna, Italy

E-mail: flavia.aleotti@unibo.it; marco.garavelli@unibo.it; irene.conti@unibo.it; luca.muccioli@unibo.it

Contents

1   Assessment of DFT functionals

MP2 and several DFT functionals were assessed against CASPT2 along both torsion and inversion pathways for the AB molecule (Figure S1), including GGA (BP86), hybrid-GGA (B3LYP, PBE0), hybrid meta-GGA (M06) and range-separated hybrid (ωB97X-D3) functionals. All DFT and MP2 calculations were performed with ORCA 4,[S1] using def2-SVP basis set, applying dispersion corrections when not already included in the original functional. The discontinuities in the torsional profiles are a consequence of the sudden geometrical change between consecutive points of the scan, which arises from the convergence to a linear geometries for some points of the scan when DFT is used (see below). MP2 recovers the dynamic correlation along the inversion path, but performs poorly along torsion, due to the lack of static correlation.

In a subsequent benchmark, we have assessed the effect of larger basis sets and the performances of different types of functionals (BP86, B3LYP, CAM-B3LYP, B2PLYP, all with def2-SVP basis set) on all the considered systems along the torsional profile (Figure
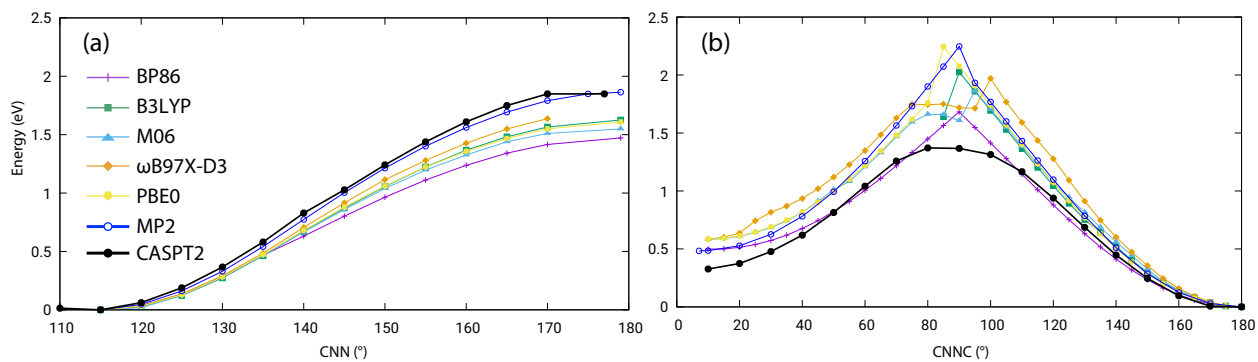
Figure S1: Assessment of several DFT functionals against CASPT2 along (a) inversion and (b) torsion pathways of AB.

S2). Our results showed negligible variations upon basis set size increase, endorsing the use of def2-SVP. Concerning the functionals, none of the considered ones delivers results close to CASPT2 (neither qualitatively nor quantitatively), confirming that the DFT error is an intrinsic consequence of the lack of multiconfigurational character, that cannot be recovered even by more refined functionals.

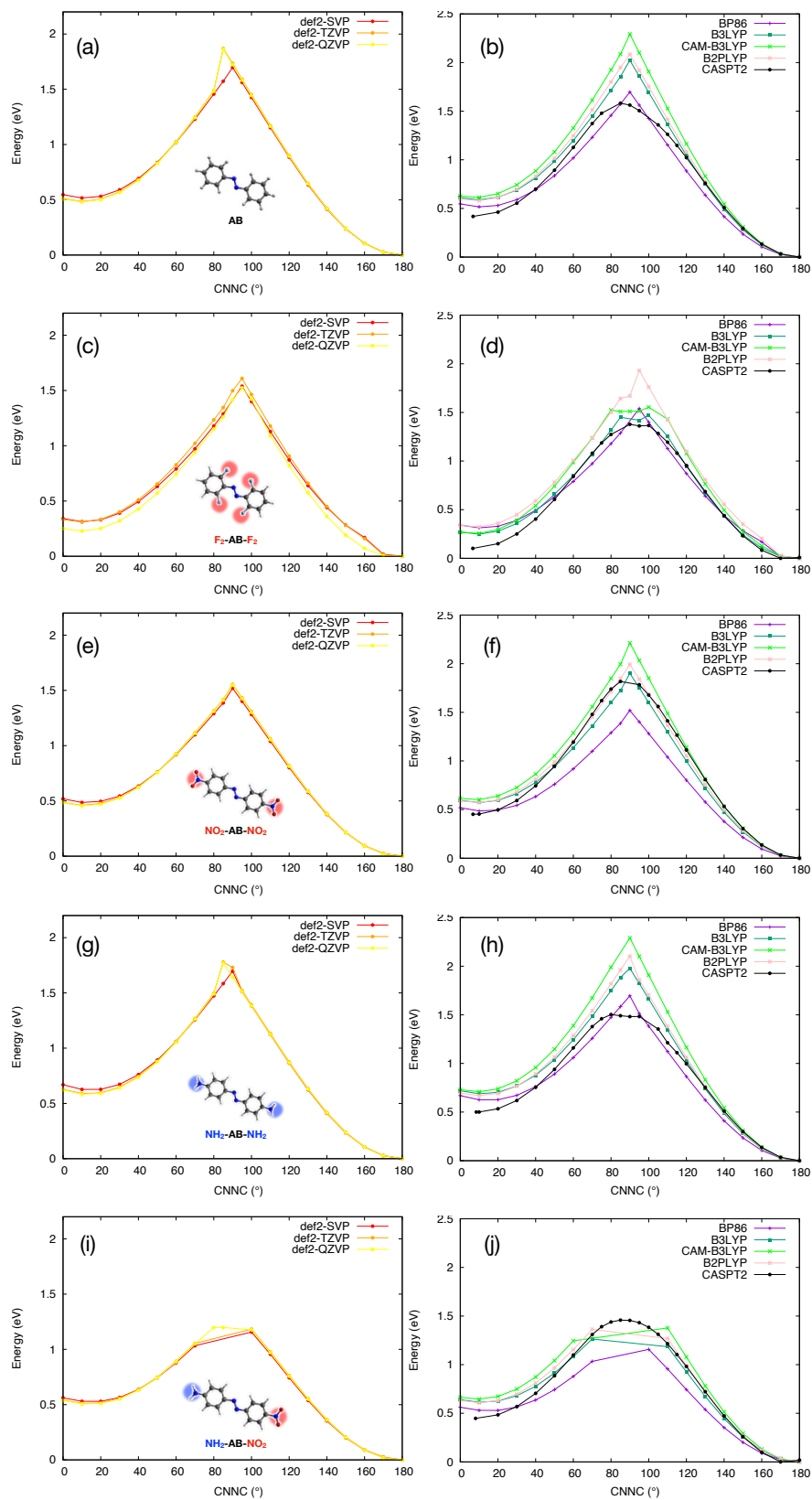Figure S2: Assessment of basis set (left) and DFT functionals (right, with def2-SVP) on AB (a,b), F_2-AB-F_2 (c,d), NO_2-AB-NO_2 (e,f), NH_2-AB-NH_2 (g,h) and NO_2-AB-NH_2 (i,j). Missing scan points are a consequence of convergence problems caused by DFT artifacts.

2 Computational details

2.1 DFT calculations

The E and Z isomers of all the considered molecules were optimized at the BP86/def2-SVP level of theory, applying Grimme's DFT-D3 dispersion correction.[S2] For the investigation of the inversion energy profile, a relaxed surface scan at the same level of theory was performed along one of the two CNN angles starting from the Z between CNN = [130°; 180°], with steps of 5°. Only in the case of NO_2-AB-NH_2, which shows two non-equivalent CNN coordinates due to asymmetric substitution of the AB backbone, both CNN bending angles were scanned. To obtain the torsional profile, two relaxed scans were performed between the Z isomer and CNNC = 40° (step 10°) and between the E isomer and 150° (step 10°), respectively. For more rotated geometries, instead, some constrained optimizations were performed to avoid the convergence to a linear TS. Indeed, DFT yields a wrong PES along torsion (due to its single-reference nature) and a too low barrier along inversion (see Figure S3 (a)). As a result, all the points of fully-relaxed scan between CNNC = 50° and CNNC = 140° land in the linear (inversion) TS, for which CNNC value is not defined. To avoid this, we have made a linear interpolation of the CNN and NNC values at the scan points CNNC = 40° and CNNC = 150° (i.e., the last points of the fully-unconstrained scans starting from Z and E isomers, respectively), and we have performed optimizations keeping the CNN/NNC values fixed at their interpolated value for CNNC = 50°, 60°, 70°, 75°, 80°, 85°, 90°, 95°, 100°, 105°, 110°, 120°, 130°and 140°. All DFT calculations were performed with ORCA 4.[S1]
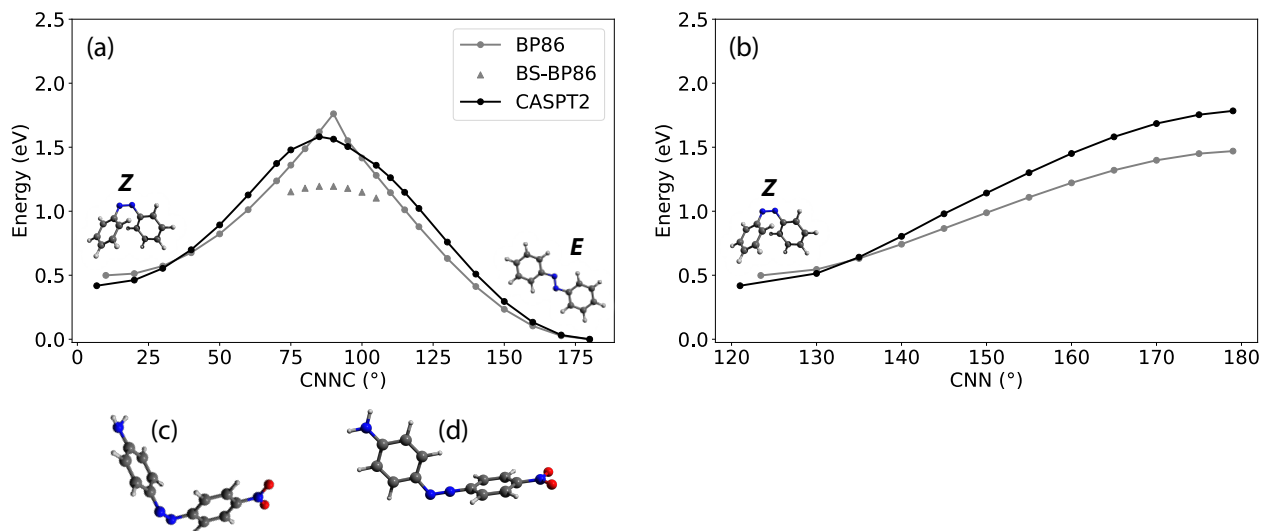
Figure S3: Comparison between DFT, BS-DFT (BP86) and CASPT2 for AB along (a) torsion and (b) inversion pathways. The structures of the CASPT2 (c) and DFT (d) fully-optimized TS are also shown.

2.2 BS-DFT calculations

For all the investigated molecules, BS-DFT (BP86/def2-SVP, applying Grimme's DFT-D3 dispersion correction[S2]) was tested along the CNNC torsion scan between CNNC = 75° and CNNC = 105° (step 5°) to converge to a broken-symmetry solution (open-shell singlet) flipping the spin of one of the two nitrogen atoms. No further constraints were applied besides the CNNC value. The results for AB are shown in Figure S3 (a). All BS-DFT calculations were performed with ORCA 4.[S1]

2.3 CASPT2 calculations

The E and Z isomers of all the considered molecules were optimized at the XMS-CASPT2 level of theory (using an imaginary shift of 0.2 a.u and without any IP/EA correction) employing the ANO-R basis set, in its R1 variant.[S3] The choice of this basis set (specifically optimized for CASSCF/CASPT2) allowed to reach high accuracy reducing the computational cost. The perturbative correction was applied on CASSCF wavefunctions obtained with an

active space of 10 electrons in 8 orbitals (3 π, 3 π^* and two N lone pairs, see Figures S4-S8), including two electronic states (S_0, S_1) in the state-averaging procedure. The π/π^* active orbitals were selected for each molecule according to the algorithm described in section 4, and we have checked that each active space remained consistent between minima and transition states for each system. The (10,8) active space size was the largest to afford CASPT2 gradients on our computational resources, and it was already used in previous studies of AB, yielding satisfactory results.[S4] We have performed fully-relaxed potential energy surface scans along CNN (inversion) and CNNC (torsion) coordinates starting from the Z isomer with the same scan steps employed for DFT scans (see previous section). For each molecule, we have performed some TS search along torsion and inversion pathways, obtaining structures in very good agreement with those from the relaxed scans (see Table SXXX). Along the CNNC scan, we have also mapped the energy of the T_1 state at XMS-CASPT2/SA1-CASSCF(10,8)/ANO-R1 level. Then, T_1 minimum and its two crossings with S_0 were fully optimized. The XMS-CASPT2/SA2-CASSCF(10,8)/ANO-R1 level of theory was also used to perform energy calculations along DFT scans. All CASPT2 calculations were performed with OpenMolcas 23.10,[S5] using analytical CASPT2 gradients for geometry optimizations and scans.
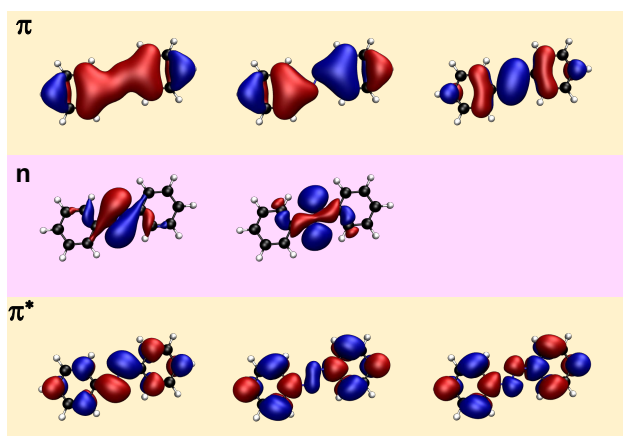

Figure S4: Active molecular orbitals (SA2-CASSCF(10,8)/ANO-R1) used for AB.

Figure S5: Active molecular orbitals (SA2-CASSCF(10,8)/ANO-R1) used for F_2-AB-F_2.
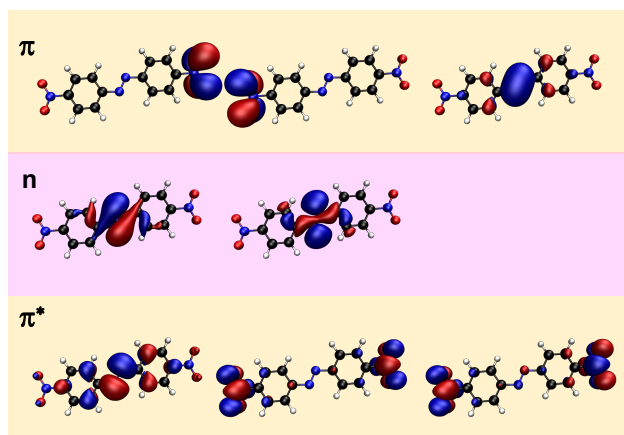
Figure S6: Active molecular orbitals (SA2-CASSCF(10,8)/ANO-R1) used for NO_2-AB-NO_2.
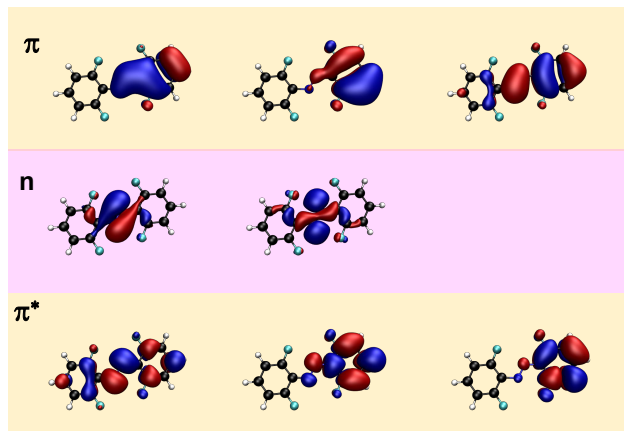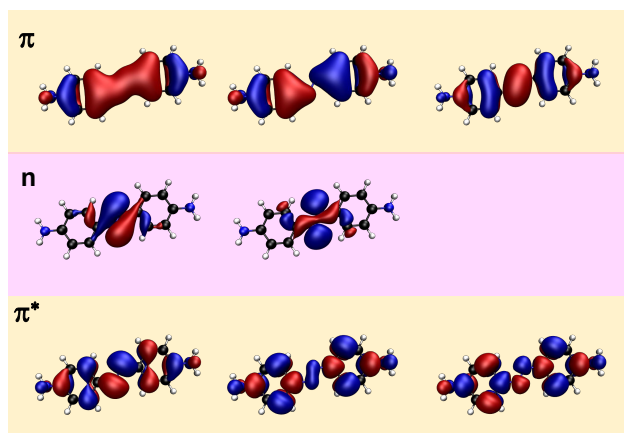

Figure S7: Active molecular orbitals (SA2-CASSCF(10,8)/ANO-R1) used for NH_2-AB-NH_2.
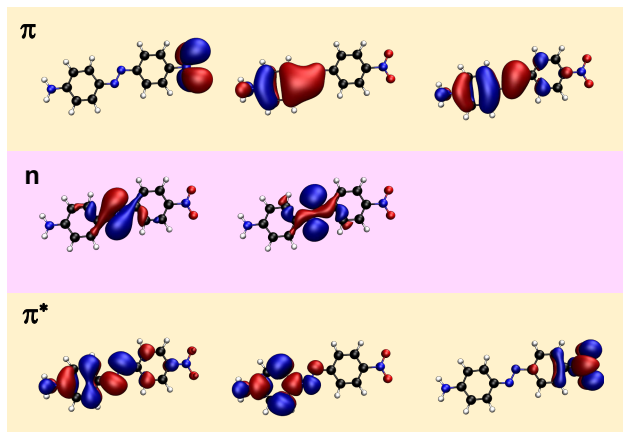
Figure S8: Active molecular orbitals (SA2-CASSCF(10,8)/ANO-R1) used for NO_2-AB-NH_2.

Table S1: Energy of torsion and inversion transition states (eV, relative to E minimum) obtained from the relaxed scan along CNNC dihedral (torsion) and CNN angle (inversion) or with fully relaxed TS search (CASPT2). The last columns report the cartesian RMSD between the two TS for every mechanism.

	TS from scan (eV)		TS optimized (eV)		RMSD (Å)	
	torsion	inversion	torsion	inversion	torsion	inversion
AB	1.582	1.784	1.584	1.789	0.004	0.031
F_2-AB-F_2	1.378	1.684	1.373	1.689	0.011	0.045
NH_2-AB-NH_2	1.503	1.960	1.504	1.965	0.006	0.039
NO_2-AB-NO_2	1.817	1.684	1.817	1.688	0.003	0.033
NO_2-AB-NH_2	1.458	1.556	1.439	1.540	0.018	0.036

3   Computational costs

Table S2 collects the computational time associated with the various steps of the full characterization of the five compounds. All calculations have been performed with OpenMolcas version 23.10 and ORCA 4 version on a Intel® Xeon® E5-2640 v4, 2.40GHz node.
CASPT2 characterization includes:

- CASSCF orbital generation (according to the algorithm described in the next section);

- Relaxed scan along torsion (23 points including E/Z minima);

- Relaxed scan along inversion (11 points).

DFT characterization includes:

- Relaxed scan along torsion (23 points including E/Z minima);

- Relaxed scan along inversion (11 points).

CASPT2@DFT characterization includes:

- DFT characterization along torsion and inversion;

- CASSCF orbital generation (according to the algorithm described in the next section);

- Calculation of CASPT2 energies along DFT scans (34 points).

Table S2: Computational time (s) required by the characterization of the considered compounds at CASPT2, DFT and CASPT2@DFT levels of theory discussed in this work.

	CASPT2				
	AB	F_2-AB-F_2	NH_2-AB-NH_2	NO_2-AB-NO_2	NO_2-AB-NH_2
Orbital generation	42870	70201	42874	32356	38241
Torsion scan	1016789	2314739	1643444	4467749	2912412
Inversion scan	708135	1412022	1079048	2209468	2329645
Total time	**1767794**	**3796962**	**2765366**	**6709573**	**5280298**
	DFT				
Torsion scan	3407	3142	3217	5342	4738
Inversion scan	2363	3057	3435	5896	4330
Total time	**5770**	**6199**	**6652**	**11234**	**9068**
	CASPT2@DFT				
CASPT2 energy	14055	30301	41584	62732	44208
Total time	**62695**	**106701**	**91110**	**106322**	**91517**

4 Automatic selection of active space

For the automatic (black-box) selection of the active space used in the abovementioned CASPT2/CASSCF calculations, we have designed the following protocol:

1. HF calculation (orbital generation);

2. Restricted Active Space SCF (RASSCF) calculation using the HF orbitals as inputs. RAS has the following composition:

   RAS1 = 20 orbitals (including HF orbitals from HOMO-19 to HOMO), with maximum 2 holes allowed during SCF procedure

   RAS2 = empty (no orbitals)

   RAS3 = 20 orbitals (including HF orbitals from LUMO to LUMO+19), with maximum 2 electrons allowed during SCF procedure

   This includes all possible single and double excitations within [HOMO-19 : LUMO+19], and accordingly relaxes the molecular orbitals;

3. Final RASSCF orbitals are sorted in order of occupation number;

4. The frontier molecular orbitals are selected from the sorted RASSCF ones to build the desired active space for CASSCF (10 electrons in 8 orbitals in this work);

5. CASSCF is performed using as inputs the orbitals selected at previous point;

6. CASPT2 is performed on CASSCF results.

RASSCF is used to perform a cheaper relaxation of a large number of HF orbitals, and at the same time their final occupations allows to identify the most relevant ones for the S_0 wavefunction (although considering only singles and doubles). Later, only a subset of orbitals most involved in the RASSCF excitations are selected for the final CASSCF calculation.

The application of this protocol to AB and the four derivatives considered for this work automatically produced the active spaces reported in Figures S4-S8. Although these five cases are not sufficient to claim its applicability to all AB derivatives, the results are promising.

5 Electrostatic potential maps

Figure S9 shows the electrostatic potential maps for all the investigated molecules at their Z isomer, torsional and inversion transition states (TS). The fluorination of ortho positions (F_2-AB-F_2) is known to stabilize the Z isomer of azobenzene by F-C electrostatic interaction[S6] (compare S9 (a) and (b)). The same effect can stabilize also the torsional TS, although to a minor extent (Figure S9 (f) and (g)).
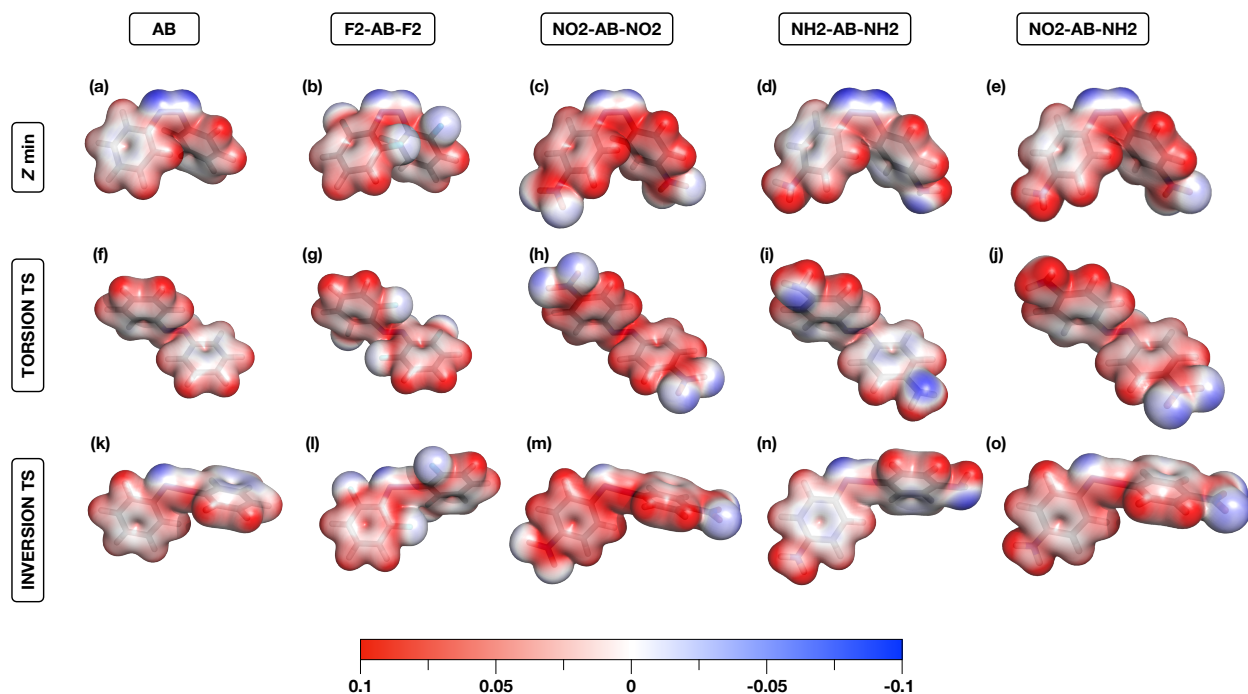
Figure S9: Electrostatic potential maps (XMS-CASPT2/SA2-CASSCF(10,8)/ANO-R1) for the investigated molecules (columns) at the Z isomer (first row), torsional TS (second row) and inversion TS (third row).

The electrostatic potential was computed from the CASPT2 charges using the LIBRETA code[S7] interfaced with Multiwfn.[S8]

6 Stabilization of linear TS by mesomeric effect

The $-NO_2$ group is known to stabilize the linear (CNN inversion) transition state by mesomeric effect[S9] (Figure S10 (a)). In a *push-pull* derivative (Figure S10 (b)), the presence of a donor group in para position on the other phenyl ring allows for further delocalization of the positive charge, enhancing the effect.
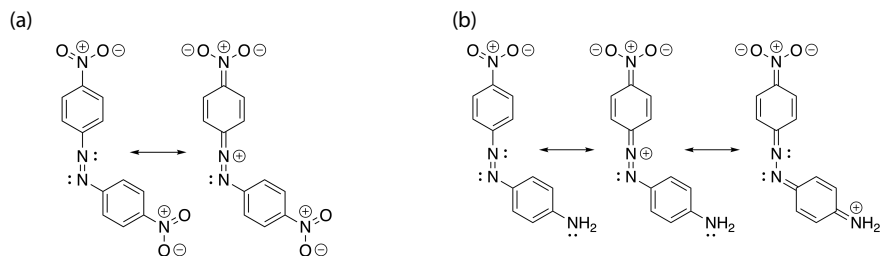
Figure S10: Resonance formulas stabilizing the linear (inversion) TS in (a) NO_2-AB-NH_2 and (b) NO_2-AB-NO_2.

7 Stabilization/destabilization of torsion TS

The non-linear (rotated) torsional TS can be stabilized in AB compounds that favor resonance formulas in which the central N−N bond becomes a single bond. The presence of the $-NO_2$ group in para position strongly destabilizes the $=N-N=$ resonance formulas due to electrostatic repulsion between the positive charges of the substituent and that delocalized on the phenyl ring (Figure S11 (a)). On the other hand, the single-bond configuration ($=N-N=$) is stabilized in NH_2-AB-NH_2 and even more in NO_2-AB-NH_2 (Figure S11 (b-c)). This effect is perfectly reflected by the trend in the torsional isomerization barriers reported in this work[i] (NO_2-AB-NO_2: 42.9 kcal/mol > AB: 37.3 kcal/mol > NH_2-AB-NH_2: 35.5 kcal/mol > NO_2-AB-NH_2: 34.4 kcal/mol)

Figure S11: Relevance of resonance formulas showing a single bond character of the central N−N bond for the considered compounds: (a) NO_2-AB-NO_2, (b) AB, (c) NH_2-AB-NH_2, (d) NO_2-AB-NH_2.

---

[i]Considering the energy barriers relative to the E isomer, to get rid of Z stabilization/destabilization effects.

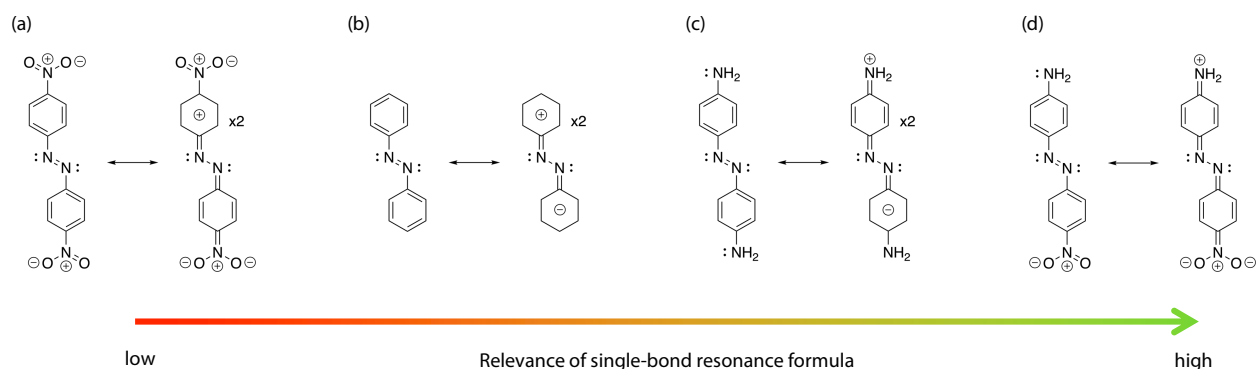# 8 Orbital energies

Tables S3 and S4 collect the energies of the frontier molecular orbitals of the five investigated molecules at their Z minimum and at the torsional transition state, respectively.

Table S3: Frontier orbital energies (eV) calculated at the Z minimum.

	HOMO-4	HOMO-3	HOMO-2	HOMO-1	HOMO	LUMO	LUMO+1	LUMO +2
CASPT2								
AB	-9.9030	-9.8867	-9.3539	-9.3147	-7.7011	0.2754	3.0869	3.4480
F_2-AB-F_2	-11.3028	-11.1722	-9.6815	-9.4960	-8.2946	-0.0672	2.9731	3.2801
NO_2-AB-NO_2	-11.4081	-10.6935	-10.3613	-10.0796	-9.0342	-0.5101	2.3954	2.6370
NH_2-AB-NH_2	-9.7912	-9.2527	-8.8799	-8.7841	-7.1816	0.5926	3.1486	3.2901
NO_2-AB-NH_2	-10.6680	-10.2813	-10.0010	-9.4932	-8.0007	-0.0179	2.8082	2.9734
BP86								
AB	-6.7601	-6.6197	-6.4395	-6.3240	-4.9254	-3.1335	-1.5690	-1.3882
F_2-AB-F_2	-6.8124	-6.6808	-6.5088	-6.4051	-5.3427	-3.4148	-1.5865	-1.5696
NO_2-AB-NO_2	-7.4060	-7.3755	-6.9310	-6.9278	-5.9653	-4.3932	-3.6186	-3.2278
NH_2-AB-NH_2	-6.2983	-6.0918	-5.1181	-5.0951	-4.0047	-2.3846	-1.1978	-0.8362
NO_2-AB-NH_2	-6.7757	-6.6408	-6.2501	-5.7506	-4.9362	-3.3466	-2.7322	-1.8403

Table S4: Frontier orbital energies (eV) calculated at the torsional transition state.

	HOMO-4	HOMO-3	HOMO-2	HOMO-1	HOMO	LUMO	LUMO+1	LUMO +2
CASPT2								
AB	-10.3069	-10.0832	-9.4777	-9.1811	-6.0341	-2.4900	3.1481	3.4567
F_2-AB-F_2	-11.4288	-10.3795	-9.8364	-9.4168	-5.4213	-2.6181	3.0265	3.3563
NO_2-AB-NO_2	-11.3839	-11.1387	-10.4535	-10.1719	-7.1291	-3.2104	2.5038	2.8616
NH_2-AB-NH_2	-10.3085	-9.0775	-8.9479	-8.9025	-5.4072	-1.7916	3.0534	3.3783
NO_2-AB-NH_2	-10.7923	-10.1066	-9.7673	-9.6739	-6.4298	-2.1693	2.6869	3.1037
BP86								
AB	-6.8019	-6.6192	-6.5548	-6.5422	-4.1847	-4.2937	-1.4306	-1.3002
F_2-AB-F_2	-7.0390	-6.8493	-6.4351	-6.4344	-4.3444	-4.3382	-1.3975	-1.3249
NO_2-AB-NO_2	-7.3058	-7.3052	-6.7896	-6.7879	-5.4441	-5.5186	-3.4042	-3.3291
NH_2-AB-NH_2	-6.1903	-6.1367	-5.2734	-5.2711	-3.1879	-3.1637	-1.0129	-0.8373
NO_2-AB-NH_2	-6.3752	-6.2917	-6.1365	-5.5586	-4.2624	-4.3335	-2.2235	-2.0872
BS-BP86 (u = spin up orbitals, d = spin down)								
AB	-6.7622 (u)	-6.6581 (u)	-6.5584 (u)	-6.4655 (u)	-4.4849 (u)	-3.7009 (u)	-1.4583 (u)	-1.2195 (u)
	-6.7633 (d)	-6.6583 (d)	-6.5568 (d)	-6.4652 (d)	-4.4845 (d)	-3.7026 (d)	-1.4581 (d)	-1.2200 (d)
F_2-AB-F_2	-7.0221 (u)	-6.8318 (u)	-6.4590 (u)	-6.3592 (u)	-4.5854 (u)	-3.8339 (u)	-1.4286 (u)	-1.2437 (u)
	-7.0216 (d)	-6.8325 (d)	-6.4577 (d)	-6.3605 (d)	-4.5843 (d)	-3.8356 (d)	-1.4283 (d)	-1.2436 (d)
NO_2-AB-NO_2	-7.3383 (u)	-7.3012 (u)	-6.8207 (u)	-6.8008 (u)	-5.6314 (u)	-4.9638 (u)	-3.3950 (u)	-3.2467 (u)
	-7.3364 (d)	-7.3031 (d)	-6.8188 (d)	-6.8027 (d)	-5.6323 (d)	-4.9636 (d)	-3.3958 (d)	-3.2462 (d)
NH_2-AB-NH_2	-6.2517 (u)	-6.0874 (u)	-5.3533 (u)	-5.1972 (u)	-3.4984 (u)	-2.8010 (u)	-1.0655 (u)	-0.7882 (u)
	-6.2536 (d)	-6.0856 (d)	-5.3533 (d)	-5.1974 (d)	-3.4971 (d)	-2.8024 (d)	-1.0643 (d)	-0.7897 (d)
NO_2-AB-NH_2	-6.5021 (u)	-6.3821 (u)	-6.1742 (u)	-5.8170 (u)	-4.3622 (u)	-4.0388 (u)	-2.3520 (u)	-1.9097 (u)
	-6.5886 (d)	-6.4023 (d)	-6.0707 (d)	-5.8275 (d)	-4.5673 (d)	-3.8306 (d)	-2.4432 (d)	-1.8024 (d)

9 Involvement of T_1 in the thermal $Z \to E$ isomerization

Previous studies on the thermal $Z{\to}E$ isomerization of azobenzene have shown that the potential energy surfaces (PESs) of S_0 and T_1 cross along the CNNC torsion coordinate,[S10,S11] and the actual involvement of T_1 in the thermal reaction has been a matter of study also for arylazopyrazole photoswitches.[S12]

As far as we know, the only experimental evidence of the role of triplets is a heavy atom effect on the activation parameters in acetonitrile, induced by adding tetra-n-butylammonium iodide,[S11] in comparison with tetra-n-butylammonium tetrafluoroborate which has no effect, though the same triplet-mediated mechanism has been invoked for the isomerization of ethylene derivatives.[S13,S14] One of the main reasons behind the scientific debate is the inability of theoretical predictions to reproduce the experimental rates, and it was shown that the failure is mostly in the sign of the reaction entropy change $\Delta S^{\ddagger}$, which is measured negative in solution (-39 $\mathrm{JK^{-1}mol^{-1}} < \Delta S^{\ddagger} < $-164 $\mathrm{JK^{-1}mol^{-1}}$ varying with solvents and substitution, see Table II of reference[S15]), but is estimated positive (or negative by few $\mathrm{JK^{-1}mol^{-1}}$) in gas phase calculations (e.g., a small but negative $\Delta S^{\ddagger}$ of -15 $\mathrm{JK^{-1}mol^{-1}}$ was extrapolated by Rietze et al.[S16] from gas phase data from reference[S17] even though this estimation is probably beyond the accuracy of the experiment).

Reimann et al.[S11] also showed that including the triplet in gas phase calculations and using non-adiabatic transition state theory (NA-TST) allows to reproduce the experimental rates (although in solvent). In fact, the presence of the transmission coefficient (γ, which depends on temperature and on the S_0/T_1 spin-orbit coupling, SOC) gives rise to an apparent extra entropy, which is large and negative for slow, spin-forbidden reactions. However, the SOC between S_0 and T_1 in azobenzene (which is estimated $\approx 20 \, \mathrm{cm}-1$ in references[S10] and[S11]), is very sensitive to the calculation method, and the NA-TST reactions rates accordingly, as underlined also in a subsequent study on arylazopyrazole photoswitches.[S12] As a side comment we also note that there exists different models for calculating the intersystem crossing rate (see e.g. references[S18–S20]), each of them producing rather different values.

In order to further investigate the role of the triplet state in the thermal isomerization of azobenzene, we have performed optimization and vibrational analysis of all the relevant points on the S_0 and T_1 potential energy surface (i.e., S_0 transition states (TS) along torsion and inversion pathways, T_1 minimum and S_0/T_1 minimum-energy crossing points (MECP)) at the XMS-CASPT2/CASSCF(10,8)/ANO-R1 level of theory (state averaging on 2 states for singlets, 1 state for the triplet). Using the CASPT2 wavefunctions, we were also able to calculate the S_0/T_1 SOC at the two MECP. Because the final rate was shown to be particularly sensitive to the SOC value used, we have also performed some more refined calculations of the SOC values at the two MECPs (level of theory: XMS-CASPT2/CASSCF(18,16)/ANO-R1 using the full π/π^* + 2n active space, see reference[S21]) for comparison. With this data, we were able to calculate the rates for all the possible Z->E isomerization mechanisms. All the optimizations, SOC and Hessian calculations were performed with OpenMolcas 23.10,[S5] while the vibrational analysis and the calculation of thermodynamic quantities were performed using Python functions from the PySCF code.[S22]

Figure S12 shows the S_0 and T_1 potential energy profiles along the torsional path and a graphical representation of the activation energies associated with the two proposed torsional mechanisms (named torsion type I and II, i.e. without or with the involvement of T_1, respectively). For the two adiabatic mechanisms (inversion and torsion type I, taking place on S_0) the rate is obtained with Eyring's original equation[S23]

$$k = \frac{k_B T}{h} \gamma \exp\left(-\frac{\Delta G^{\ddagger}}{RT}\right) \tag{1}$$

where k_B, h and R are Boltzmann, Planck and the universal gas constants (respectively), T is the temperature, $\Delta G^{\ddagger}$ is the activation free energy and γ is a transmission coefficient. For the case of the adiabatic passage through a transition state, γ can be calculated through
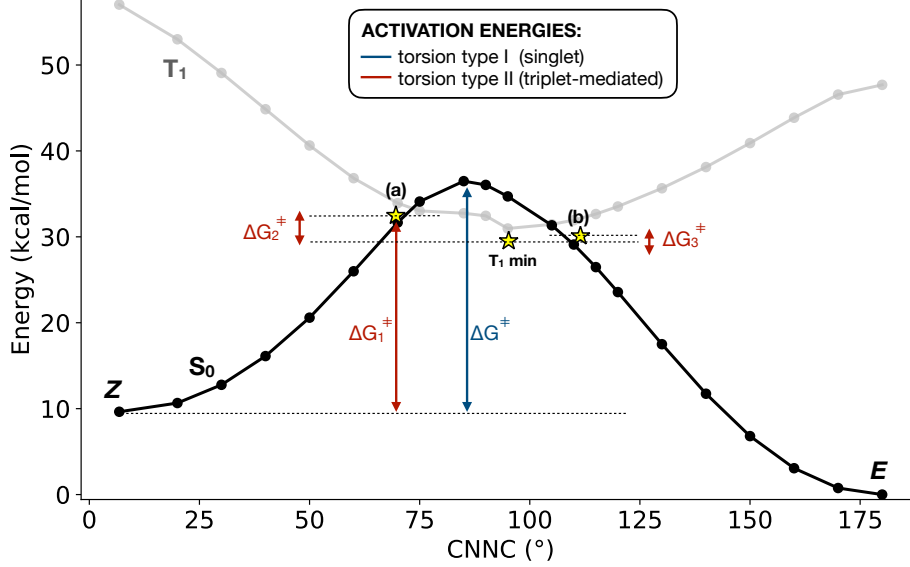
Figure S12: Potential energy profiles of S_0 (black) and T_1 (grey) of AB along the CNNC torsional path (relaxed surface scan on S_0, see computational details). The stars mark the position of the fully relaxed T_1 minimum and S_0/T_1 MECPs (points (a) and (b)). The arrows show the activation energies associated with the two proposed torsional mechanisms (type I and II, following reference[S11]).

Wigner's expression for the shallow-tunneling correction factor[S24]

$$\gamma = \frac{\hbar\beta \times \omega^{\ddagger}/2}{\sin\left(\hbar\beta \times \omega^{\ddagger}/2\right)} \tag{2}$$

where $\hbar$ is the reduced Planck constant, $\omega^{\ddagger}$ is the value of the frequency which is imaginary at the saddle point and $\beta = 1/(k_B T)$. In practice, γ is typically close to unity for these kinds of reactions.

Concerning torsion type II (i.e., triplet-mediated), it is modelled as a two-step reaction passing through T_1 minimum and mediated by two S_0/T_1 crossings, which originate three energy barriers (see $\Delta G_1^{\ddagger}$, $\Delta G_2^{\ddagger}$ and $\Delta G_3^{\ddagger}$ in Figure S12). Indeed, for this reaction we assume the following kinetic scheme

$$Z \underset{k_2}{\overset{k_1}{\rightleftharpoons}} T_1 \text{ min} \xrightarrow{k_3} E \tag{3}$$

in which, after the first ISC event (taking place at point (a) and associated to $\Delta G_1^{\ddagger}$, see

Figure S12), the molecule relaxes to the T_1 minimum, and from there it can undergo the second ISC event in both directions (i.e., it can either proceed to the E isomer overcoming $\Delta G_3^{\ddagger}$ at point (b), or return back to Z over $\Delta G_2^{\ddagger}$ at point (a)). Instead, the formation of the E isomer is assumed as an irreversible step, owing to its high thermodynamical stability. This is equivalent to the reaction scheme 1 of reference[S25] for which the reaction rate is shown to be (eq. 11 therein):

$$k = \left[\frac{1}{k_1} + \frac{k_2}{k_1 k_3} + \frac{1}{k_3} \right]^{-1} \tag{4}$$

The single rate constants k_1, k_2 and k_3 can be calculated through equation (1), but in which the γ factor is calculated as a function of temperature and S_0/T_1 SOC magnitude associated to the spin-forbidden transition. Here, we have used the NA-TST γ equation reported in reference[S11] (eq. 2 therein). Eventually, for the calculation of the free energy at the two S_0/T_1 MECPs we have used an effective Hessian[ii] obtained as

$$\mathbf{H_{eff}} = \frac{|\mathbf{F_{S_0}}|\mathbf{H_{T_1}} + |\mathbf{F_{T_1}}|\mathbf{H_{S_0}}}{|\Delta \mathbf{F}|} \tag{5}$$

(where $\mathbf{F}_i$ and $\mathbf{H}_i$ are the gradient vector and Hessian matrix of the i-th electronic state, and $\Delta \mathbf{F}$ is the gradient difference at the MECP). The gradient difference direction was projected out of $\mathbf{H_{eff}}$ (together with translations and rotations) before diagonalization, yielding 3N-7 vibrational frequencies for each MECP.

Then, using CASPT2 data, we have calculated the rates associated to the three proposed mechanisms (at 298 K) using equations (1) and (2) (for inversion and torsion type I) or equations (1), (4) and eq. 2 from reference[S11] (for the non adiabatic rotation type II). The results are shown in Table S5.

We note that, for torsion type II, the rate-determining step is the passage through the

---

[ii] in contrast to eq. 8 of reference[S11] we have used the + combination of Hessians, as required for the case of a peaked crossing (see reference[S26] for the derivation).

Table S5: Thermodynamical parameters and rate constants (at 298.15K) for the three proposed thermal $Z{\to}E$ isomerization mechanisms. The definition of the apparent entropy $\Delta\tilde{S}^{\ddagger}$ is the same as in reference[S11]).

Mechanism	$\Delta H^{\ddagger}$ (kJ/mol)	$\Delta S^{\ddagger}$ (J/(mol× K))	$\Delta G^{\ddagger}$ (kJ/mol)	SOC (cm^{-1})	γ	$\Delta\tilde{S}^{\ddagger}$ (J/(mol× K))	k (s^{-1})
inversion	126.7	+2.1	126.1	-	1.000	+2.1	5.123e-10
torsion (type I)	100.5	-13.5	104.6	-	1.000	-13.5	2.970e-06
torsion (type II)	83.9	-13.1	87.8	17.039	9.663e-03	-51.6	2.472e-05
				13.692	6.240e-03	-55.3	1.598e-05
				10.000	3.328e-03	-60.5	8.570e-06
				5.000	8.321e-04	-72.0	2.148e-06
experiment[S27] (25°C)	115.2	+1.4	109.0	-	-	-	-
experiment[S27] (100°C)	114.6	+1.2	107.5	-	-	-	-

first MECP (i.e., first ISC event) owing to the much larger barrier, and therefore the final rate is almost completely determined by the activation energy $\Delta G_1^{\ddagger}$ and by the associated SOC value[iii]. The latter was calculated to be $17.039\,\mathrm{cm}^{-1}$ using the (10,8) active space. This value is only a bit smaller than the previously reported values obtained at CASSCF level[S10,S11] ($18 < \mathrm{SOC} < 23\,\mathrm{cm}^{-1}$). However, we found out that using a larger active space (see before), the SOC values decreases to $13.692\,\mathrm{cm}^{-1}$. The decreasing SOC values obtained with increasingly accurate calculations suggest that we might be still overestimating the S_0/T_1 coupling. For this reason, we have calculated the rate constant associated to type II rotation also using SOC values of 10 and $5\,\mathrm{cm}^{-1}$ (see Table S5). The sensitivity of the estimate of the transmission coefficient γ on the SOC value and, therefore, on the rate constant is evident from Table S5: the triplet-mediated mechanisms is the fastest by one order of magnitude when using $\mathrm{SOC} = 17.039\,\mathrm{cm}^{-1}$, but it slows down until it becomes competitive with (or even slower than) the rotation type I when $\mathrm{SOC} < 10\,\mathrm{cm}^{-1}$.

A further element that we have to take into account is the dependence of the rate constants on temperature. Because γ for the non adiabatic reaction (torsion type II) decreases

---

[iii]We note that our equations and kinetic model are different from those used in reference,[S11] in which the relaxation to T_1 minimum and the reversibility of the ISC at MECP point (a) were not considered. However, due to the asymmetry in the AB potentials (see Figure S12) there is a significant difference in the free energies of the two MECPs, with $G_{(a)}^{\ddagger} >> G_{(b)}^{\ddagger}$. As a consequence, we have verified that (for AB) the application of the model presented in reference[S11] leads to rates for torsion type II identical to those given ones in Table S5.

significantly with temperature (see equation 2 of reference[S11]) while it remains constant ≈ 1 for the adiabatic torsion (type I), the latter mechanism dominates at high temperature. We have calculated the rate constants for the various mechanisms at several temperature values, in order to produce an Arrhenius plot (Figure S13) that we can compare with those from experimental gas-phase studies.[S17,S27] According to our calculations, the triplet-mediated mechanism is the fastest only below 373 K (100°C). However, the two sets of experimental data (purple and green lines in Figure S13) seem to follow pretty well the rates calculated for torsion type I (blue line in Figure S13). This suggests that we might be overestimating the rate of the non adiabatic reaction (probably due to approximations in NA-TST model or due to an overestimation of S_0/T_1 SOC, as suggested before) and the adiabatic torsion type I might be the most relevant even at room (or at least not too high) temperature.
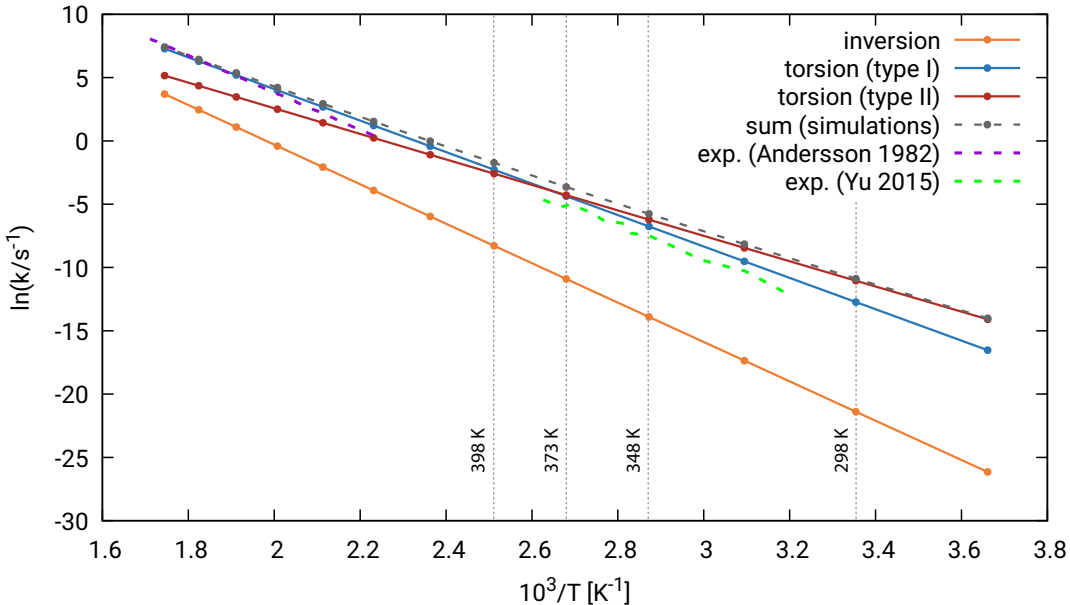

Figure S13: Arrhenius plot for the thermal $Z{\to}E$ azobenzene isomerization in gas phase using CASPT2 data for the inversion mechanisms (orange), torsion type I mechanism (blue) and triplet-mediated torsion type II mechanism (red, using SOC = $13.692\,\mathrm{cm}^{-1}$). The overall rates from simulations (sum of the constants for the three mechanisms) is also shown in dark gray. For comparison, we also plot data from experiments in vapor phase, extracted from Arrhenius plots in references[S27] and.[S17]

Eventually, in order to investigate how much our previous considerations could be extended to the other azobenzene derivatives, we have mapped the T_1 state (both at DFT and

CASPT2 level) and the S_0/T_1 SOC (CASPT2) along CNNC torsion for all the other derivatives. In addition, we have optimized (at CASPT2 level) T_1 and the two S_0/T_1 MECPs for each of them. The results are shown in Figure S14. We conclude that

- DFT (BP86/def2-SVP) always underestimates the triplet energy, with the largest error observed for NO_2-AB-NO_2;

- the two S_0/T_1 crossing points are asymmetric for all the derivatives, with the MECP on the Z side being higher in energy and therefore rate-determining for torsion type II in all cases;

- for the purpose of a large-scale investigation (for which CASPT2 optimizations are not affordable), the simple evaluation of T_1 energy along the BP86/def2-SVP CNNC ground-state scan (with constrained CNN bending angles) gives an acceptable approximation of the S_0/T_1 crossing points, especially in the case of the kinetically-relevant one (i.e., the one on the Z side, see Figure S14)

- S_0/T_1 SOC is always maximum at the E and Z minima where the two states are far apart in energy. Closer to the torsional TS, S_0 acquires some $n\pi^*$ character (due to the mixing with S_1, see discussion in the main text) which lowers the coupling with T_1 ($n\pi^*$ character) in agreement with El-Sayed rule;

- the energy and SOC profiles of all the four substituted derivatives are qualitatively similar to those of pristine AB, however the position (and energy) of the S_0/T_1 crossing can vary. NO_2-AB-NO_2 shows the largest difference between the activation energies of torsion type I (TS on S_0) and type II (S_0/T_1 crossing, see Figure S14 (d)) while NH_2-AB-NH_2 shows the smallest difference (Figure S14 (c)). Because the distance from the TS influences also the SOC value (see previous point) we can foresee that torsion type II could be more relevant in the case of NO_2-AB-NO_2.
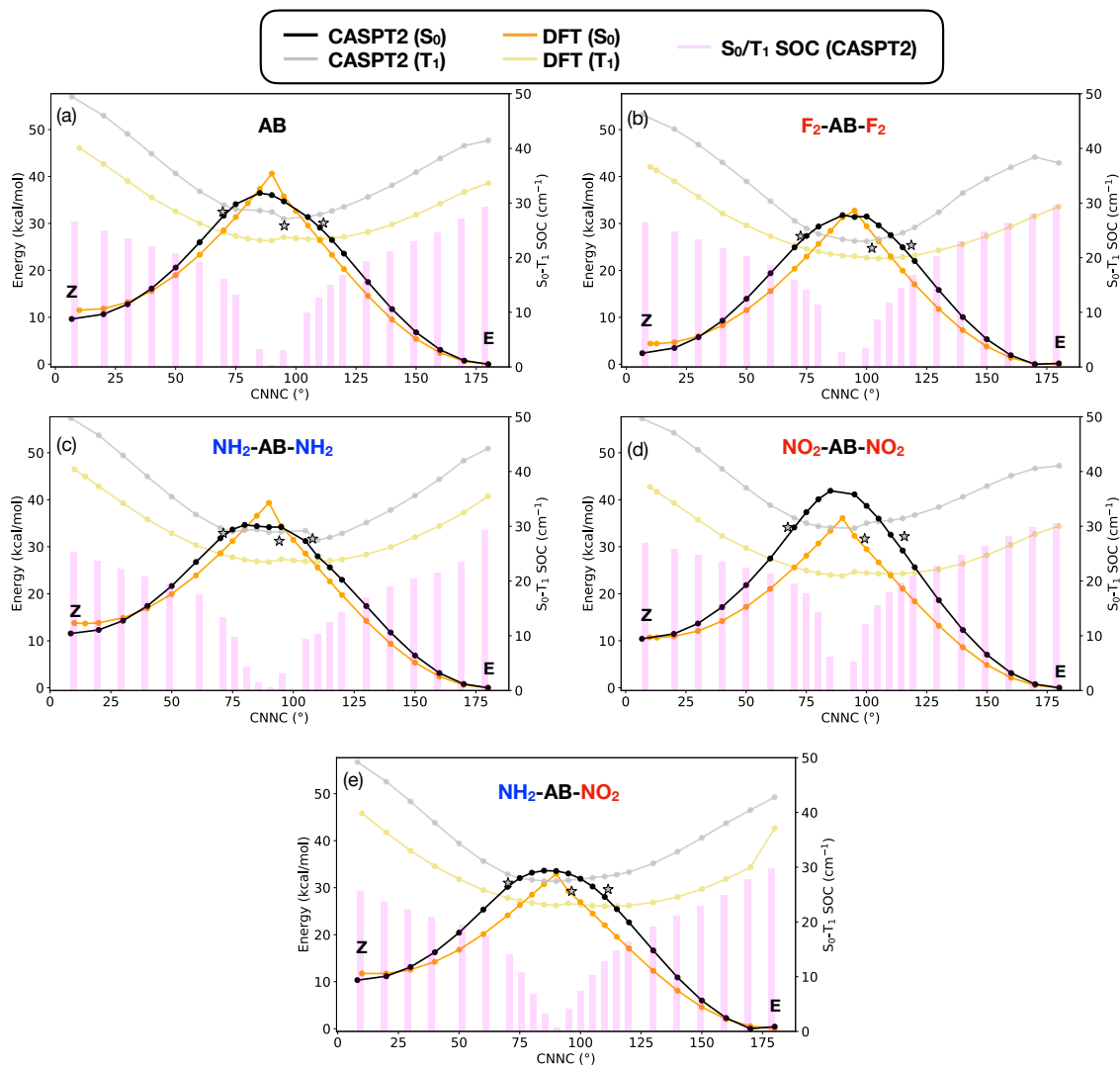
Figure S14: Potential energy profiles along CNNC torsion (relaxed scan on S_0) for (a) AB, (b) F_2-AB-F_2, (c) NH_2-AB-NH_2, (d) NO_2-AB-NO_2 and (e) NO_2-AB-NH_2 at CASPT2 (S_0: black, T_1: grey) and DFT (S_0: orange, T_1: yellow) levels of theory. The S_0/T_1 spin-orbit coupling (SOC, pink bars), calculated at CASPT2 level, is also reported for every point of the scan. The gray stars mark the CASPT2-optimized T_1 minima and S_0/T_1 minimum-energy crossing points.

References

(S1) Neese, F.; Wennmohs, F.; Becker, U.; Riplinger, C. The ORCA quantum chemistry program package. *The Journal of Chemical Physics* **2020**, *152*.

(S2) Grimme, S.; Antony, J.; Ehrlich, S.; Krieg, H. A consistent and accurate ab initio parametrization of density functional dispersion correction (DFT-D) for the 94 elements H-Pu. *The Journal of Chemical Physics* **2010**, *132*.

(S3) Zobel, J. P.; Widmark, P.-O.; Veryazov, V. The ANO-R basis set. *Journal of Chemical Theory and Computation* **2019**, *16*, 278–294.

(S4) Casellas, J.; Bearpark, M. J.; Reguero, M. Excited-State Decay in the Photoisomerisation of Azobenzene: A New Balance between Mechanisms. *ChemPhysChem* **2016**, *17*, 3068–3079.

(S5) Li Manni, G.; Fdez. Galván, I.; Alavi, A.; Aleotti, F.; Aquilante, F.; Autschbach, J.; Avagliano, D.; Baiardi, A.; Bao, J. J.; Battaglia, S.; others The OpenMolcas Web: A community-driven approach to advancing computational chemistry. *Journal of Chemical Theory and Computation* **2023**, *19*, 6933–6991.

(S6) Saccone, M.; Siiskonen, A.; Fernandez-Palacio, F.; Priimagi, A.; Terraneo, G.; Resnati, G.; Metrangolo, P. Halogen bonding stabilizes a cis-azobenzene derivative in the solid state: a crystallographic study. *Acta Crystallographica Section B: Structural Science, Crystal Engineering and Materials* **2017**, *73*, 227–233.

(S7) Zhang, J. LIBRETA: Computerized optimization and code synthesis for electron repulsion integral evaluation. *Journal of Chemical Theory and Computation* **2018**, *14*, 572–587.

(S8) Lu, T. A comprehensive electron wavefunction analysis toolbox for chemists, Multiwfn. *The Journal of Chemical Physics* **2024**, *161*.

(S9) Dokić, J.; Gothe, M.; Wirth, J.; Peters, M. V.; Schwarz, J.; Hecht, S.; Saalfrank, P. Quantum chemical investigation of thermal cis-to-trans isomerization of azobenzene derivatives: substituent effects, solvent effects, and comparison to experimental data. *The Journal of Physical Chemistry A* **2009**, *113*, 6763–6773.

(S10) Cembran, A.; Bernardi, F.; Garavelli, M.; Gagliardi, L.; Orlandi, G. On the Mechanism of the cis- trans Isomerization in the Lowest Electronic States of Azobenzene: S0, S1, and T1. *Journal of the American Chemical Society* **2004**, *126*, 3234–3243.

(S11) Reimann, M.; Teichmann, E.; Hecht, S.; Kaupp, M. Solving the azobenzene entropy puzzle: Direct evidence for multi-state reactivity. *The Journal of Physical Chemistry Letters* **2022**, *13*, 10882–10888.

(S12) Singer, N. K.; Schlögl, K.; Zobel, J. P.; Mihovilovic, M. D.; González, L. Singlet and triplet pathways determine the thermal Z/E isomerization of an arylazopyrazole-based photoswitch. *The Journal of Physical Chemistry Letters* **2023**, *14*, 8956–8961.

(S13) Magee, J. L.; Shand, W. J.; Eyring, H. Non-adiabatic Reactions. Rotation about the Double Bond*. *Journal of the American Chemical Society* **1941**, *63*, 677–688.

(S14) Lin, M. C.; Laidler, K. J. Some aspects of cis–trans-isomerization mechanisms. *Canadian Journal of Chemistry* **1968**, *46*, 973–978.

(S15) Asano, T.; Okada, T.; Shinkai, S.; Shigematsu, K.; Kusano, Y.; Manabe, O. Temperature and pressure dependences of thermal cis-to-trans isomerization of azobenzenes which evidence an inversion mechanism. *Journal of the American Chemical Society* **1981**, *103*, 5161–5165.

(S16) Rietze, C.; Titov, E.; Lindner, S.; Saalfrank, P. Thermal isomerization of azobenzenes: on the performance of Eyring transition state theory. *Journal of Physics: Condensed Matter* **2017**, *29*, 314002.

(S17) Yu, X.; Wang, Z.; Buchholz, M.; Füllgrabe, N.; Grosjean, S.; Bebensee, F.; Bräse, S.; Wöll, C.; Heinke, L. cis-to-trans isomerization of azobenzene investigated by using thin films of metal–organic frameworks. *Physical Chemistry Chemical Physics* **2015**, *17*, 22721–22725.

(S18) Valiev, R. R.; Cherepanov, V. N.; Baryshnikov, G. V.; Sundholm, D. First-principles method for calculating the rate constants of internal-conversion and intersystem-crossing transitions. *Physical Chemistry Chemical Physics* **2018**, *20*, 6121–6133.

(S19) Valentine, A. J.; Li, X. Toward the evaluation of intersystem crossing rates with variational relativistic methods. *The Journal of Chemical Physics* **2019**, *151*.

(S20) Marian, C. M. Spin–orbit coupling and intersystem crossing in molecules. *Wiley Interdisciplinary Reviews: Computational Molecular Science* **2012**, *2*, 187–203.

(S21) Aleotti, F.; Soprani, L.; Nenov, A.; Berardi, R.; Arcioni, A.; Zannoni, C.; Garavelli, M. Multidimensional potential energy surfaces resolved at the RASPT2 level for accurate photoinduced isomerization dynamics of azobenzene. *Journal of chemical theory and computation* **2019**, *15*, 6813–6823.

(S22) Sun, Q.; Zhang, X.; Banerjee, S.; Bao, P.; Barbry, M.; Blunt, N. S.; Bogdanov, N. A.; Booth, G. H.; Chen, J.; Cui, Z.-H.; others Recent developments in the PySCF program package. *The Journal of Chemical Physics* **2020**, *153*.

(S23) Eyring, H. The activated complex and the absolute rate of chemical reactions. *Chemical Reviews* **1941**, *17*.

(S24) Zhang, Y.; Rommel, J. B.; Cvitaš, M. T.; Althorpe, S. C. Shallow-tunnelling correction factor for use with Wigner–Eyring transition-state theory. *Physical Chemistry Chemical Physics* **2014**, *16*, 24292–24300.

(S25) Park, C. Analysis of Chemical Kinetics of Multistep Reactions by Mean Reaction Time. *ACS Omega* **2024**,

(S26) Lykhin, A. O.; Kaliakin, D. S.; DePolo, G. E.; Kuzubov, A. A.; Varganov, S. A. Nonadiabatic transition state theory: Application to intersystem crossings in the active sites of metal-sulfur proteins. *International Journal of Quantum Chemistry* **2016**, *116*, 750–761.

(S27) Andersson, J.-Å.; Petterson, R.; Tegnér, L. Flash photolysis experiments in the vapour phase at elevated temperatures I: spectra of azobenzene and the kinetics of its thermal cis-trans isomerization. *Journal of Photochemistry* **1982**, *20*, 17–32.